The Orbit of NGC 5907 ULX-1

Andrea Belfiore,[1] Ruben Salvaterra,[1] Lara Sidoli,[1] Gian Luca Israel,[2] Luigi Stella,[2] Andrea De Luca,[1] Sandro Mereghetti,[1] Paolo Esposito,[3,1] Fabio Pintore,[4] Antonino D'Aì,[4] Guillermo Rodrìguez Castillo,[4] Dominic J. Walton,[5,6] Felix Fürst,[7] Danilo Magistrali,[8] Anna Wolter,[9] and Matteo Imbrogno[10,2,11]

[1]INAF, Istituto di Astrofisica Spaziale e Fisica Cosmica, Via Alfonso Corti 12, I-20133, Milano, Italy
[2]INAF, Osservatorio Astronomico di Roma, Via Frascati 33, I-00078, Monteporzio Catone, Italy
[3]Scuola Universitaria Superiore IUSS Pavia, Palazzo del Broletto, Piazza Della Vittoria 15, I-27100, Pavia, Italy
[4]INAF, Istituto di Astrofisica Spaziale e Fisica Cosmica, Via Ugo La Malfa 153, I-90146, Palermo, Italy
[5]Centre for Astrophysics Research, University of Hertfordshire, College Lane, Hatfield AL10 9AB, UK
[6]Institute of Astronomy, University of Cambridge, Madingley Road, Cambridge CB3 0HA, UK
[7]European Space Agency (ESA), European Space Astronomy Centre (ESAC), Camino Bajo del Castillo s/n, 28692 Villanueva de la Cañada, Madrid, Spain
[8]Universidad Pontificia Comillas Madrid-ICAI, Calle de Alberto Aguilera 25, 28015, Madrid, Spain
[9]INAF, Osservatorio Astronomico di Brera, Via Brera 28, I-20121, Milano, Italy
[10]Dipartimento di Fisica, Università degli Studi di Roma "Tor Vergata", via della Ricerca Scientifica 1, I-00133 Rome, Italy
[11]Università degli Studi di Roma "La Sapienza", Piazzale Aldo Moro 5, I-00185, Roma, Italy

ABSTRACT

We report on the orbit of the binary system powering the most extreme ultraluminous X-ray pulsar known to date: NGC 5907 ULX-1 (hereafter ULX1). ULX1 has been the target of a substantial multi-instrument campaign, mainly in the X-ray band, but no clear counterparts are known in other bands. Although ULX1 is highly variable and pulsations can be transient (regardless of the source flux), the timing data collected so far allow us to investigate the orbit of this system. We find an orbital period $P_{orb} = 5.7^{+0.1}_{-0.6}$ d and a projected semi-axis $A_1 = 3.1^{+0.8}_{-0.9}$ lts. The most likely ephemeris is: $P_{orb} = 5.6585(6)$ d, $A_1 = 3.1(4)$ lts, and the epoch of ascending nodes passage is: $T_{asc} = 57751.37(5)$ MJD. However, there are 6 similar solutions, acceptable within 3σ. We find further indications that ULX1 is a high-mass X-ray binary. This implies that we are observing its orbit face-on, with an inclination < 5 deg.

1. INTRODUCTION

NGC 5907 ULX-1 (ULX1) is the most luminous member of the known ultraluminous X-ray pulsars (PULXs), peaking at an apparent luminosity of $L_{X,peak} \sim 10^{41}$ erg s^{-1}. PULXs are an emerging class of accreting X-ray pulsars with luminosity far in excess of the Eddington limit for a neutron star. This is a sub-class of ultraluminous X-ray sources (ULXs), i.e. X-ray sources, located off-center of their host galaxy, whose isotropic luminosity is greater than 10^{39} erg s^{-1} (Walton et al. 2022; Tranin et al. 2023; for recent reviews see King et al. 2023; Pinto & Walton 2023). PULXs are accreting pulsars, likely in high mass X-ray binary (HMXB) systems, and thus are neutron stars orbiting a stellar companion. Their accretion geometry is not spherical and their magnetic field is so strong that the Eddington limit – which assumes spherical symmetry and Thomson cross-section – does not formally apply. Still, it remains a useful point of reference for comparison with other X-ray binary systems. Given the extreme nature of PULXs, it is

Corresponding author: Andrea Belfiore
andrea.belfiore@inaf.it

important to investigate the nature of their companions and to measure the orbital parameters of these systems, as they reflect the conditions under which accretion at such extreme rates can occur. Because the detection of pulsations depends on several factors (including pulsed fraction, photon statistics, and background level), other known ULXs may yet turn out to be PULXs, as we keep observing them (King & Lasota 2016; Pintore et al. 2017; Walton et al. 2018).

After the discovery of pulsations with XMM-Newton and NuSTAR (Israel et al. 2017a), ULX1 has been regularly monitored with the Neil Gehrels Swift Observatory and observed on numerous occasions with XMM-Newton, NuSTAR, and Chandra (Fürst et al. 2023). The neutron star powering ULX1 shows strong long-term variability, exhibiting a high state that can last for years ($L_{X,peak} \sim 10^{41} \, erg \, s^{-1}$), during which its flux is modulated over a period of 78 d (Walton et al. 2016), as well as a low state ($L_X < 10^{39} \, erg \, s^{-1}$) during which a spatially extended X-ray nebula is revealed (which is otherwise drowned out by the emission from the point source; Belfiore et al. 2020). The source can transition between these high- and low-flux states within days (Walton et al. 2015). The pulsed fraction of ULX1 seems to vary randomly across different observations and its spin period P_{spin} evolves noticeably, driven by the strong torque that results from the accretion of matter at a very high rate (which is also responsible for its extreme luminosity; Fürst et al. 2023). The earliest detection of pulsations revealed a spin period of 1.43 s in 2003, with the neutron star having subsequently been spun up to spin periods of 1.14 s in 2014 and 0.95 s in 2017. This erratic behavior hampers timing studies of the pulsar.

Because the host galaxy, NGC 5907, is nearly edge-on, our line of sight to ULX1 is heavily obscured by dust. Optical/NIR searches for its counterpart have thus proven difficult. We are therefore forced to rely only on X-ray timing of the pulsar to infer the orbital parameters of this system. A first estimate of the period (P_{orb}), projected semiaxis ($A_1 = a_{ns} \cdot \sin i$), and epoch of ascending nodes (T_{asc}) of the orbit of the neutron star came together with the discovery of pulsations (Israel et al. 2017a). Such an analysis was based on two NuSTAR observations taken in July 2014, with a baseline of 4.7 days. They report, at 1 σ confidence, $P_{orb} = 5.3^{+2.0}_{-0.9}$ d and $A_1 = 2.5^{+4.3}_{-0.8}$ lts. However, at 3 σ confidence, only lower limits on $A_1 > 1.4$ lts and $P_{orb} > 4.0$ d were obtained, whereas upper limits rely on physical considerations about the mass of the companion.

In this paper we consider all of the observations taken so far with XMM-Newton and NuSTAR and derive an updated orbital ephemeris. Sec. 2 describes the data used for this paper and how they were selected. Sec. 3 describes the timing analysis that leads to our results, presented in Sec. 4. A discussion follows in Sec. 5, and conclusions are drawn in Sec. 6.

2. OBSERVATIONS AND DATA PREPARATION

Timing ULX1 requires sufficient photon statistics and good time resolution, which restricts our analysis to the data obtained by two X-ray observatories: NuSTAR (Harrison et al. 2013) and XMM-Newton (Jansen et al. 2001). The rapid and erratic spin evolution of ULX1 does not allow for coherent timing on long timescales (more than a few weeks), while on short timescales the intrinsic behaviour of the pulsar (e.g. the accretion-driven spin-up) can account for any linear trend in spin period. Therefore we must rely on clusters of 2 or more observations, all taken within a couple of weeks of each other, during which pulsations are detected. Any non-linearity in the spin evolution within each observation cluster can be ascribed, to a first approximation, to the orbit of the system.

So far, 3 clusters of observations that meet the above requirements are available (see table 1): 3 observations in 2014 (cluster A; these are the data that led to the initial discovery of pulsations and to the first orbital ephemeris), 2 observations in 2017 (cluster B), and 3 observations in 2019 (cluster C).

The XMM-Newton observations were taken with the the EPIC-PN camera (Strüder et al. 2001) in Full Frame mode, and thus have a time resolution of 73.4 ms. We do not consider the EPIC-MOS data because its time resolution is not sufficient for the timing analysis of a ~ 1 s pulsar. We used the XMM-Newton Scientific Analysis System (SAS v21.0 Gabriel et al. 2004) to reprocess and filter the events, and to correct their time of arrival to the Solar System barycenter (using the DE200 ephemeris). We adopt the position obtained for ULX1 with Chandra (Sutton et al. 2013): R.A. = 15h 15m 58.62s ± 0.01s, Dec = +56° 18' 10.3" ± 0.1" (J2000). We applied standard quality filters and excluded periods of high background, as recommended by the XMM-Newton team. We kept all the events within 30″ of the position of ULX1 with energies $E > 1$ keV. These criteria maximise the strength of the pulsed signal for this particular pulsar (Israel et al. 2017a).

The NuSTAR observations used data from both focal plane modules (FPMA and FPMB) which have a time resolution of 2 μs. They were reduced with the NuSTAR Data Analysis Software (NuSTARDAS v2.1.2). We applied the standard

cluster	obs. ID	observatory	date	duration (ks)	photons
A	0729561301	XMM-Newton	2014-07-09	42 (42)	12879
A	80001042002	NuSTAR	2014-07-09	57	3297
A	80001042004	NuSTAR	2014-07-12	56	3291
B	0804090301	XMM-Newton	2017-07-02	40 (32)	3394
B	0804090401	XMM-Newton	2017-07-04	36 (36)	2221
C	0824320201	XMM-Newton	2019-06-12	60 (59)	12216
C	0824320301	XMM-Newton	2019-06-19	49 (49)	9069
C	0824320401	XMM-Newton	2019-06-26	64 (54)	7854

Table 1. X-ray observations used in our analysis. For XMM-Newton, in parentheses is the net exposure time, after the removal of high background periods. The number of photons is measured after all filters have been applied. The baselines for the 3 clusters are: 404 ks for cluster A, 222 ks for cluster B, and 1271 ks for cluster C.

quality filters recommended by the NuSTAR team, and kept all the events within $49''$ of the position of ULX1 with energies in the $3-15$ keV range.

We again shifted the time of arrival of the photons to the Solar System barycenter.

3. DATA ANALYSIS

The pulse profile of ULX1 is well approximated by a sinusoid. We construct a model for the evolution of the period of this sinusoid and fit it directly to the time of arrival of each photon, using an unbinned likelihood analysis (Israel et al. 2017a, suppl. mat.). The most likely set of parameters in our model is our best-fit solution. We then perturb the optimal solution by varying each single parameter. As we shift one parameter we profile the likelihood by maximising it over all the other parameters. We then estimate the uncertainties by measuring the drop in likelihood and applying Wilks' theorem (Cowan et al. 2011).

Our model accounts for an evolution of the intrinsic spin period of the pulsar (due to accretion or other torques) and the Doppler modulation induced by the orbital motion. We assume that within each cluster of observations (taken less than 2 weeks apart) the intrinsic evolution of the spin period P is linear, i.e. its time derivative $\dot{P}$ is constant. We do not assume any relation between the spin parameters taken in different clusters of observations as the accretion rate is variable and hardly predictable. Any non-linearity in the spin evolution observed within a cluster of observations is ascribed to the orbital modulation. We assume that the orbit is circular and that its parameters (the projected semi-axis A_1, the orbital period P_{orb} and the epoch of ascending node passage T_{asc}) do not change across different clusters.

Our assumption of a circular orbit is not granted, a priori. However, we can take it as a first order approximation. In particular, because most often the pulsar is far from periapsis, we expect a very limited bias due to this assumption. As more timing data become available, this model can be extended to account for an eccentric orbit.

It is clear that the secular spin evolution is intrinsic, because no orbit (not even around a supermassive black hole) could account for a change in the spin period of $> 10\%$, as observed for ULX1 (Fürst et al. 2023). However, on short timescales the shift in $\dot{P}$ induced by a binary orbit can be of the same order as the intrinsic $\dot{P}$. Therefore this observable is fully degenerate with the unknown intrinsic spin-up (or spin-down) and we cannot build upon that to constrain the orbit.

We start by considering each cluster of observations by itself. This analysis provides weak independent constraints on the 3 orbital parameters. In order to minimize the correlation between P_{orb} and T_{asc}, we keep T_{asc} as close as possible to the midpoint of each cluster. We focus on A_1 and P_{orb}, by comparing their estimates in each set of observations and combining them. The analysis of each cluster maximises the likelihood over all the other parameters: P, $\dot{P}$ and the orbital phase T_{asc}.

Afterwards, we shift our estimates of T_{asc} to a common epoch (close to the midpoint of all data) by adding or subtracting an integer number of full orbits. Generally, given a pair A_1 and P_{orb}, the values of T_{asc} shifted from clusters A and C do not match. Forcing them to be the same, while considering both data sets at once, introduces some aliases in P_{orb} separated by:

$$\Delta P_{orb} \simeq \frac{P_{orb}^2}{T_C - T_A} \simeq 0.018 \, \text{d} \tag{1}$$

ID	TS	N_σ	R_A	R_B	R_C	P_{orb} [d]	A_1 [lts]	T_{asc} [MJD]
320	543.83	-	262.76	76.53	202.92	5.6585(6)	3.1(4)	57751.37(5)
343	541.53	1.5	263.80	76.78	199.32	5.2753(3)	2.5(3)	57753.65(5)
338	540.11	1.9	263.19	76.79	198.51	5.3538(3)	2.5(3)	57751.05(5)
348	539.41	2.1	263.13	75.55	199.12	5.1992(2)	2.6(2)	57750.97(4)
325	539.36	2.1	262.09	75.98	199.68	5.5702(4)	2.7(3)	57754.06(4)
333	536.21	2.7	262.00	74.71	197.90	5.4348(2)	2.5(1)	57753.83(3)
351	535.05	2.9	261.88	73.50	198.10	5.1546(1)	2.7(1)	57753.52(1)

Table 2. Coherent orbital solutions acceptable at the 3-σ level in a single parameter. The ID corresponds to the number of full orbits between the observations in clusters A and C. The drop in test statistic (TS) from the optimum solution asymptotically follows a χ^2 distribution with 1 degree of freedom, and is converted to σ units (i.e. N_σ). We report also the Rayleigh TS (a measure of the strength of the signal) for each cluster of observations (R_A, R_B, and R_C). The orbital parameters are: the orbital period P_{orb}, the projected semi-axis A_1, and the epoch of ascending nodes T_{asc}. All the uncertainties (in parentheses after the last digit) are at 3σ on a single parameter, with respect to the most likely solution (ID 320).

Finally, we examine all these aliases, considering data from all 3 clusters at the same time.

4. RESULTS

The likelihood analysis within each cluster of observations provides non-linear constraints on the orbital parameters. In particular, only clusters A and C provide independent estimates of all the 3 orbital parameters. The analysis of cluster B, which has a much shorter baseline, provides looser constraints, in which each of the orbital parameters is fully degenerate with the other two. Therefore, we used only the analysis of clusters A and C to derive a first estimate for A_1 and P_{orb} (see fig. 1).

We then combined the two estimates of A_1 and P_{orb}, without enforcing coherence in the orbital phase between the two epochs. The most likely values are $P_{orb} = 5.66\,\mathrm{d}$ and $A_1 = 3.10\,\mathrm{lts}$ and, at 3σ, $5.0\,\mathrm{d} < P_{orb} < 5.8\,\mathrm{d}$ and $2.3\,\mathrm{lts} < A_1 < 4.0\,\mathrm{lts}$. These values are consistent to within 1σ with the individual estimates obtained for each of the clusters when considered independently (again see fig. 1). Therefore, our approximation with a circular orbit seems to be justified.

Finally, we fixed the orbital phase between the two main clusters, A and C, and also incorporated the data from cluster B. As described above, in sec. 3, forcing the coherence in orbital phase between clusters A and C induces aliases in P_{orb}. Many of these aliases can be ruled out as they imply a value of T_{asc} which is not consistent with the observations in cluster B. Only 7 aliases are acceptable to within 3σ, and one of them stands out (ID 320, corresponding to 320 full orbits between T_A and T_C, see table 2).

The most likely value of the orbital parameters, for alias 320, is: $P_{orb} = 5.6585(6)\,\mathrm{d}$, $A_1 = 3.1(4)\,\mathrm{lts}$, and $T_{asc} = \mathrm{MJD}\,57751.37(5)$. The reported uncertainty, at 3σ on a single parameter of interest, is in parentheses after the last digit. As noted previously, T_{asc} is taken close to the midpoint of the observing baseline, minimising the correlation between P_{orb} and T_{asc}. The correlation between P_{orb} and A_1 does not depend on our choice of T_{asc} (see fig. 2).

From these constraints, we can derive some other parameters of the system and its geometry: the Roche lobe radius and the inclination of the orbital plane. These parameters depend on the mass of the neutron star, M_{ns} and the mass of its companion $M_c = q \cdot M_{ns}$ (where q is the mass ratio of the binary components). We take 3 representative values of $M_{ns} = 1.4$, 1.8, $2.2\,M_\odot$ and plot these quantities for a range of M_c (see fig. 3). We note that the dependence of our results on M_{ns} is very weak. For $M_{ns} = 1.8\,M_\odot$, we indicate with a shaded band the uncertainty, at 3σ, considering any of the 7 acceptable aliases in P_{orb}.

We estimate the Roche lobe radius R_l from the semi-major axis of the orbit, a, obtained from P_{orb} through Kepler's third law:

$$R_l = f(q) \cdot \left(\frac{GM_{ns}}{4\pi^2}\right)^{\frac{1}{3}} (1+q)^{\frac{1}{3}} P_{orb}^{\frac{2}{3}} \simeq 2.062 \frac{q^{\frac{2}{3}}(1+q)^{\frac{1}{3}}}{0.6q^{\frac{2}{3}} + \ln\left(1+q^{\frac{1}{3}}\right)} \left(\frac{M_{ns}}{M_\odot}\right)^{\frac{1}{3}} \left(\frac{P_{orb}}{\mathrm{d}}\right)^{\frac{2}{3}} R_\odot \tag{2}$$

where we adopted the approximation $R_l \simeq f(q) \cdot a$ (Eggleton 1983). The upper panel of fig. 3 shows the relation $R_l(M_c)$ for our estimate of P_{orb}.

We infer the inclination i of the orbital plane with respect to the line of sight by comparing a, obtained from P_{orb}, and the observed $A_1 = \frac{q}{1+q} a \sin i$:

$$\sin i = \left(\frac{GM_{ns}}{4\pi^2}\right)^{-\frac{1}{3}} \frac{(1+q)^{\frac{2}{3}}}{q} P_{orb}^{-\frac{2}{3}} A_1 = 0.102 \frac{(1+q)^{\frac{2}{3}}}{q} \left(\frac{M_{ns}}{M_\odot}\right)^{-\frac{1}{3}} \left(\frac{P_{orb}}{\mathrm{d}}\right)^{-\frac{2}{3}} \left(\frac{A_1}{\mathrm{lts}}\right) \tag{3}$$

The lower panel of fig. 3 shows the relation $i\,(M_c)$ for our estimate of P_{orb} and A_1. The lack of eclipses or dips in the light curve of ULX1, instead observed for M51 ULX7 (Vasilopoulos et al. 2021; Hu et al. 2021), implies that $\sin i < \sqrt{1 - f^2\,(q)}$, hence $i < 78\deg$. If $M_c > 5M_\odot$, then the orbit must be nearly face-on, with $i < 5\deg$.

5. DISCUSSION

We have undertaken a multi-epoch X-ray analysis of the ULX pulsar NGC 5907 ULX-1(ULX1) in order to place updated constraints on its orbital parameters by means of X-ray timing. This information is key to understanding the nature of this remarkable binary system, and can only be accessed via such studies in the X-ray band given that the distance to the source and the level of obscuration towards it have prevented the detection of any stellar counterpart at other wavelengths (e.g. Heida et al. 2019). Using our updated constraints for ULX1, we start by comparing its orbital and spin period (P_{orb} and P_{spin}, respectively) with those of other X-ray binaries containing a pulsar (Corbet 1984), see fig. 4. We also included in the plot the other PULXs with a firm estimate of their orbital period: M82 X-2 (Bachetti et al. 2014); M51 ULX-7 (Rodríguez Castillo et al. 2020); NGC 7793 P13 (Israel et al. 2017b; Fürst et al. 2016, 2021); Swift J0243.6+6124 (Wilson-Hodge et al. 2018; Tsygankov et al. 2018); RX J0209.6-7427 (Vasilopoulos et al. 2020; Chandra et al. 2020; Hou et al. 2022); SMC X-3 (Townsend et al. 2017; Liu et al. 2022).

Although this plot cannot convey the full complexity of the behavior of these sources, it captures some traits that distinguish different classes of objects (color coded in fig. 4). These are classified by looking at the companion and considering a broader set of parameters, like luminosity and variability, spectral shape/features, orbital shape and spin-up (see Chaty 2022, for a recent review). Low-mass X-ray binaries (LMXBs) have donors with mass $M_d < 1\,M_\odot$, are mostly found to have compact orbits and the accretors spin at high rates. HMXBs have donors with mass $M_d > 5\,M_\odot$, their orbits are larger and the accretors generally have longer spin periods. PULXs are in the central region of the Corbet diagram, on the lower end of P_{spin} and P_{orb} of HMXBs.

The PULXs neighboring ULX1 in the Corbet diagram are M82 X-2 and M51 ULX-7, which are both known to be HMXBs. M82 X-2 has a mass function $f(M) > 5.2\,M_\odot$ (Bachetti et al. 2014). M51 ULX-7 has a mass function $f(M) > 8\,M_\odot$, (Rodríguez Castillo et al. 2020) and candidate OB supergiant (OBsg) counterparts (Earnshaw et al. 2016). Their variability patterns show some similarity to ULX1 although they are fainter. Other PULXs, like the Galactic Swift J0243.6+6124 and RX J0209.6-7427 have larger P_{orb} and P_{spin}. Both of them have a Be companion and show a markedly different variability pattern: they show a burst at periastron and occasionally this burst can briefly surpass the limit of 10^{39} erg s^{-1} (i.e. they do not exhibit these extreme luminosities for extended periods, in contrast to ULX1 and many of the other ULX pulsars).

Exploring the other pulsar binaries with parameters similar to ULX1, we find that these are generally interpreted as HMXBs accreting through a disk. The formation of a disk demands a compact orbit, and therefore a short P_{orb} (Tauris & van den Heuvel 2023). A disk is required to attain a very large secular spin-up and to reach a short P_{spin}. This explains their behavior, common also to M82 X-2 and M51 ULX-7: persistent high luminosity and strong spin-up over long periods.

Indeed, the closest source to ULX1 is SMC X-1, a HMXB thought to be disk-fed, with a spin period $P_{spin} = 0.71$ s, an orbital period $P_{orb} = 3.89$ d, and a B0 supergiant companion (Falanga et al. 2015). It is variable, its luminosity can reach up to the Eddington limit and it spins up constantly over several years (Brumback et al. 2022). Its pulsations are transient even in a high state, just like ULX1(Pike et al. 2019). Two other peculiar sources are also close to ULX1 in the Corbet diagram: Her X-1, with a $2\,M_\odot$ donor, and GRO J1744-28, known for its peculiar bursting behavior. However, they are both accreting below their Eddington limits and their phenomenology does not match that of ULX1.

Our estimate of P_{orb}, the known $P_{spin} \sim 1$ s, and the analogy with similar systems leads us to interpret ULX1 as a HMXB, potentially with an OBsg companion, accreting through a disk onto a neutron star. This interpretation is consistent with the size of the Roche lobe inferred in eq. 2 (see fig. 3). A main sequence star would severely underfill its Roche lobe given the orbital parameters we find for ULX1. A red giant could fill its Roche lobe if it has a core mass $> 0.195\,M_\odot$ (Rappaport et al. 1995). However, a highly super-Eddington regime (exceeding the Eddington limit by a factor ~ 30) can only be sustained if $P_{orb} \simeq 1$ d (Rappaport & Joss 1997). Therefore, unless a much more efficient
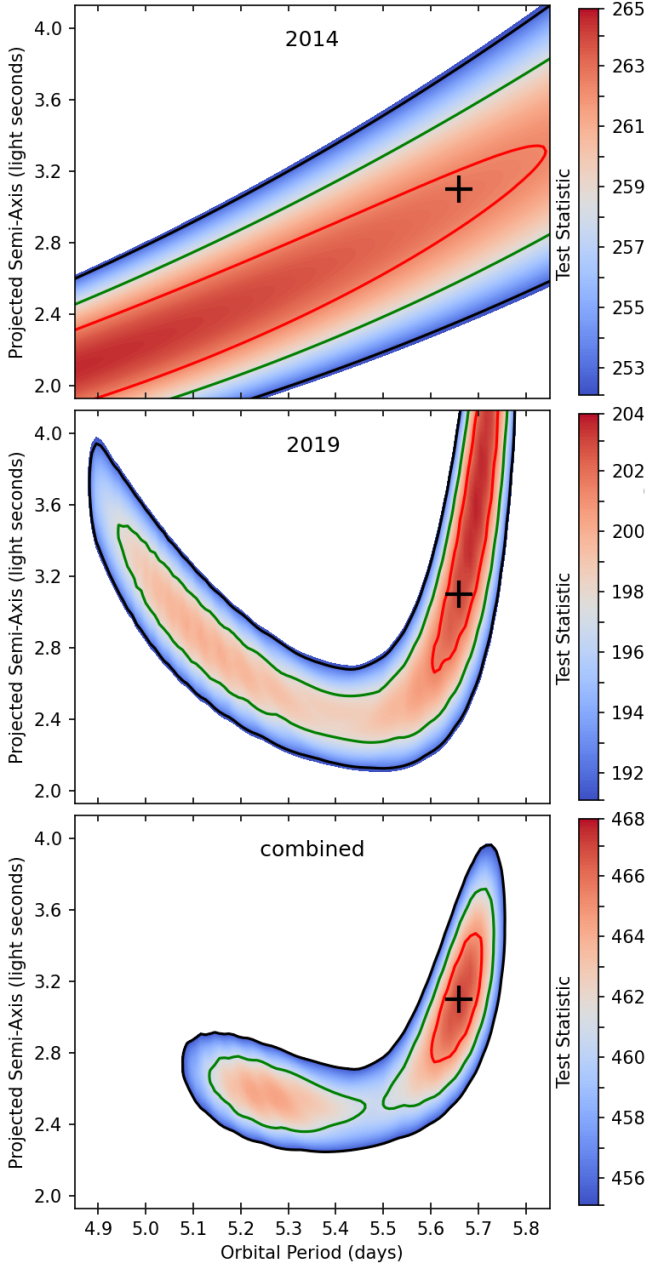
Figure 1. Estimates of the orbital period (P_{orb}, on the X-axis) and the projected semi-axis (A_1, on the Y-axis) of the orbit of ULX1. These estimates are profiled over the orbital phase (T_{asc}). The upper panel comes from the observation cluster A, the central panel from the observation cluster C, and the bottom panel combines the above two estimates (without fixing T_{asc} between them). Some aliasing is visible in the central panel (propagated to the bottom panel). A black cross marks the most likely value of $P_{orb} = 5.66$ d and $A_1 = 3.10$ lts, from the combined estimate shown in the bottom panel. Level curves indicate the 1-σ (red), 2-σ (green), and 3-σ (black) contours, for 2 degrees of freedom.

configuration can be devised, that is also compatible with a $P_{orb} \simeq 5.7$ d, a red giant companion is ruled out. OBsg and Be companions to ULX1 could fill their Roche lobes, being largely affected by factors such as rotation, metallicity, and magnetic field. A stable super-Eddington regime in which mass is transferred on a nuclear timescale can indeed be sustained for a supergiant companion, provided that its outer layer has a large metallicity gradient (Quast et al.
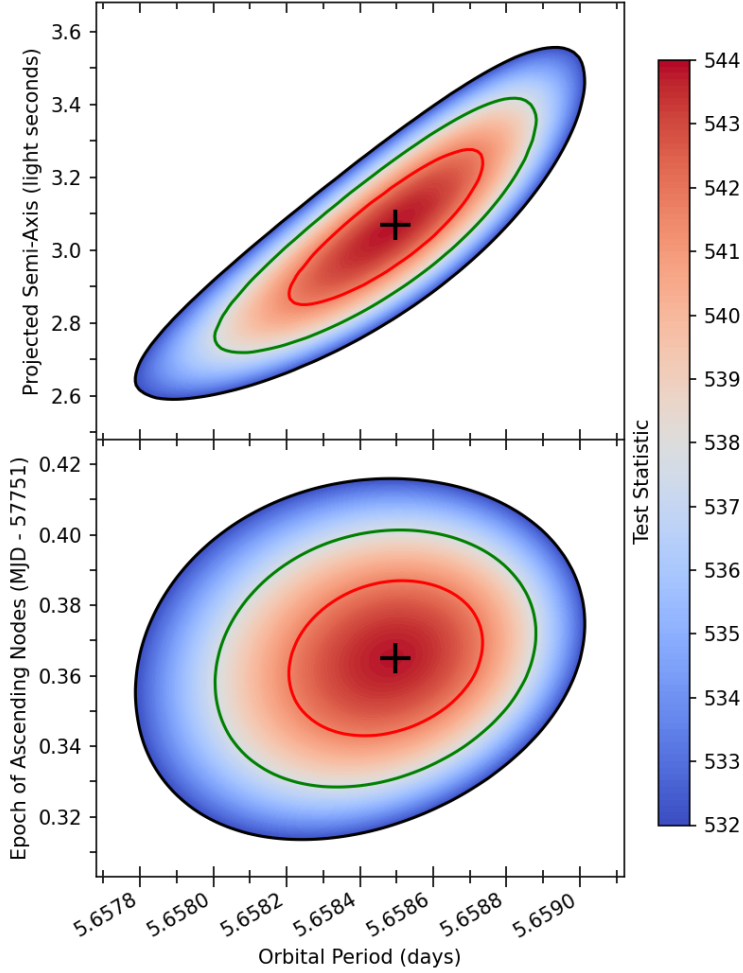
Figure 2. Estimates of the orbital parameters for the most likely alias (ID 320 in table 2) in the orbital period (P_{orb}, on the X-axis) for ULX1 based on our final, combined analysis. The upper panel shows the projected semi-axis (A_1) on the Y-axis. The lower panel shows the epoch of passage of the ascending nodes (T_{asc}) on the Y-axis. The black cross marks the most likely orbital ephemeris. Level curves indicate the 1-σ (red), 2-σ (green), and 3-σ (black) contours, for 2 degrees of freedom.

2019). This is consistent with the timescale required to fill up a nebula with hot plasma, that can explain the diffuse emission observed around ULX1 (Belfiore et al. 2020).

6. CONCLUSION

We have used all the available X-ray data on ULX1 to extract an updated orbital ephemeris. We analysed groups of observations clustered in time, initially without enforcing coherence in the orbital phase between them. We estimated the orbital period as $P_{orb} = 5.7^{+0.1}_{-0.6}$ d and the projected semi-axis as $A_1 = 3.1^{+0.8}_{-0.9}$ lts. This improves on the previous estimate by Israel et al. (2017a) where, at the same confidence level, only lower limits were given. Therefore, as already suspected, the 78 d periodicity of ULX1 (Walton et al. 2016) is not an orbital modulation.

We subsequently tried to work out a complete ephemeris by enforcing coherence in the orbital phase between groups of observations. We found 7 solutions, mutually exclusive, that are compatible with our measure of P_{orb} and A_1 reported above. The most likely ephemeris is: $P_{orb} = 5.6585(6)$ d, $A_1 = 3.1(4)$ lts, and epoch of ascending nodes passage $T_{asc} = 57751.37(5)$ MJD. A specific ephemeris is needed to assign an orbital phase to each observation, enabling future phase-resolved analyses of the available data. To resolve the remaining ambiguity over the precise orbital parameters, new and carefully-devised timing observations are needed. Any new independent ephemeris would provide a measure of the evolution of P_{orb}, as already done for several other HMXBs (Falanga et al. 2015) and recently also claimed for M82 X-2 (Bachetti et al. 2022). Because the orbital decay increases with the mass loss rate of the
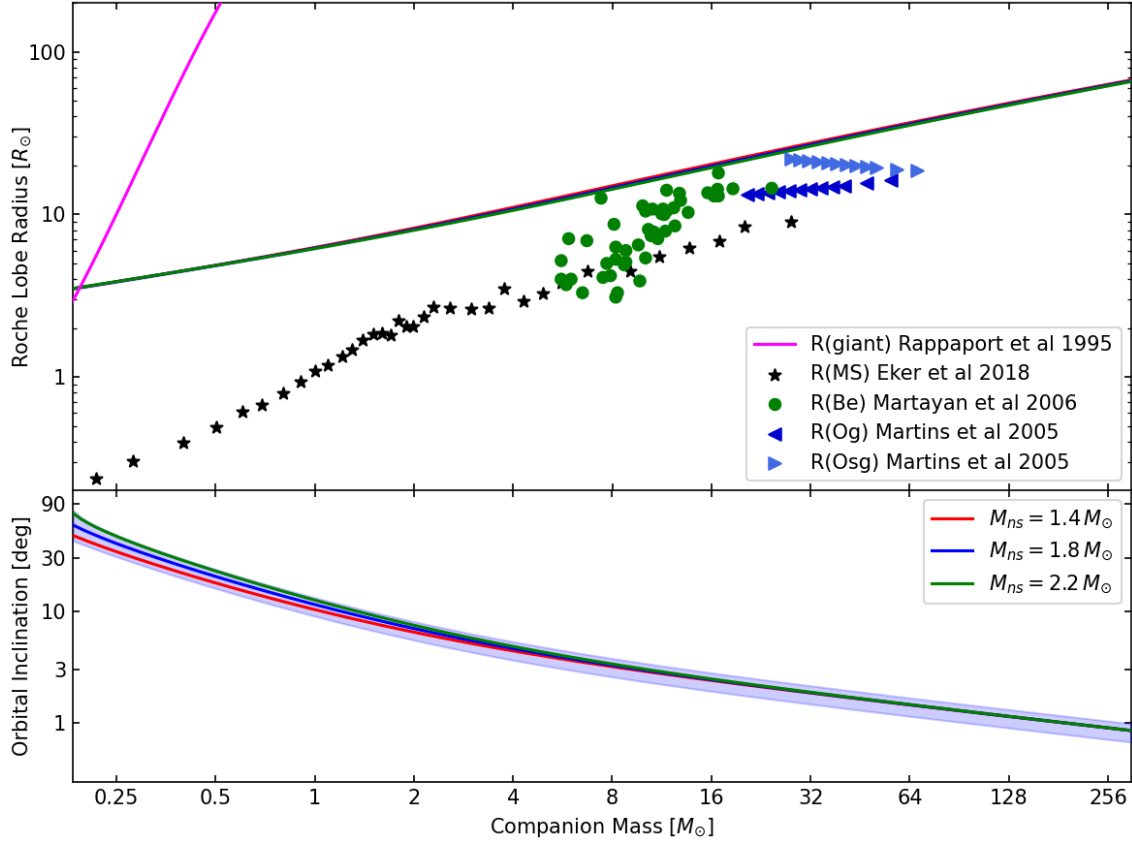
Figure 3. Geometrical parameters of the ULX1 system for 3 values of the mass of the neutron star ($M_{ns} = 1.4, 1.8, 2.2\,M_\odot$, red, blue and green lines, respectively) depending on the mass of the companion, M_c, on the X-axis. Shaded regions cover the 3-σ uncertainty ranges on the orbital parameters, assuming $M_{ns} = 1.8\,M_\odot$. **Upper panel**: on the Y-axis is the Roche lobe radius R_l in $R_\odot$ units (see eq. 2). Stellar radii (R_{star}) are also reported for different masses and stellar types for comparison (data from Rappaport et al. (1995); Eker et al. (2018); Martayan et al. (2006); Martins et al. (2005)). For mass transfer to occur $R_{star} \simeq R_l$. This rules out a main-sequence companion. **Lower panel**: on the Y-axis is the system inclination (see eq. 3). Unless M_c is very low, the orbit is ∼face-on.

donor (Quast et al. 2019), temporal baselines comparable to the existing coverage could be sufficient to detect these changes.

Based on our updated results for its orbit, we argue that ULX1 is a HMXB that contains a neutron star accreting at extreme rates through a disk from an OBsg donor. This implies that the orbit is nearly face-on with an inclination $i < 5\,\mathrm{deg}$.

APPENDIX

Figure 4. Distribution of the orbital period (P_{orb}, in days, on the X-axis) versus spin period (P_{spin}, in seconds, on the Y-axis) for known pulsars in X-ray binaries. The data shown are from Fortin et al. (2023), Neumann et al. (2023), Avakyan et al. (2023), Liu et al. (2005) and Esposito et al. (2016). Symbols and colors correspond to the legend, where SyXB indicates symbiotic X-ray binaries and SFXT indicates supergiant fast X-ray transients. We labelled all the PULXs that currently have a firm estimate of P_{orb} as well as some other systems which lie at a position close to that of ULX1 in this diagram.

## A. ORBITAL PARAMETERS FOR ALL THE ACCEPTABLE EPHEMERIDES

The main text includes a plot (fig. 2) that shows the correlation between the orbital parameters for the most likely orbital ephemeris (which we refer to as ID 320). We report here similar plots for all the other ephemerides listed in Table 2 which, while less likely, are all formally acceptable within the $3\,\sigma$ level when compared against the best-fit solution (see Figures 5 and 6). All the contour levels refer to the most likely ephemeris, displayed in fig. 2, and therefore share the same colorbar.

REFERENCES

Avakyan, A., Neumann, M., Zainab, A., et al. 2023, A&A, 675, A199

Bachetti, M., Harrison, F. A., Walton, D. J., et al. 2014, Nature, 514, 202

Bachetti, M., Heida, M., Maccarone, T., et al. 2022, ApJ, 937, 125

Belfiore, A., Esposito, P., Pintore, F., et al. 2020, Nature Astronomy, 4, 147

Brumback, M. C., Grefenstette, B. W., Buisson, D. J. K., et al. 2022, ApJ, 926, 187

Chandra, A. D., Roy, J., Agrawal, P. C., & Choudhury, M. 2020, MNRAS, 495, 2664

Chaty, S. 2022, Accreting Binaries; Nature, formation, and evolution (IOP Publishing), doi:10.1088/2514-3433/ac595f

Corbet, R. H. D. 1984, A&A, 141, 91
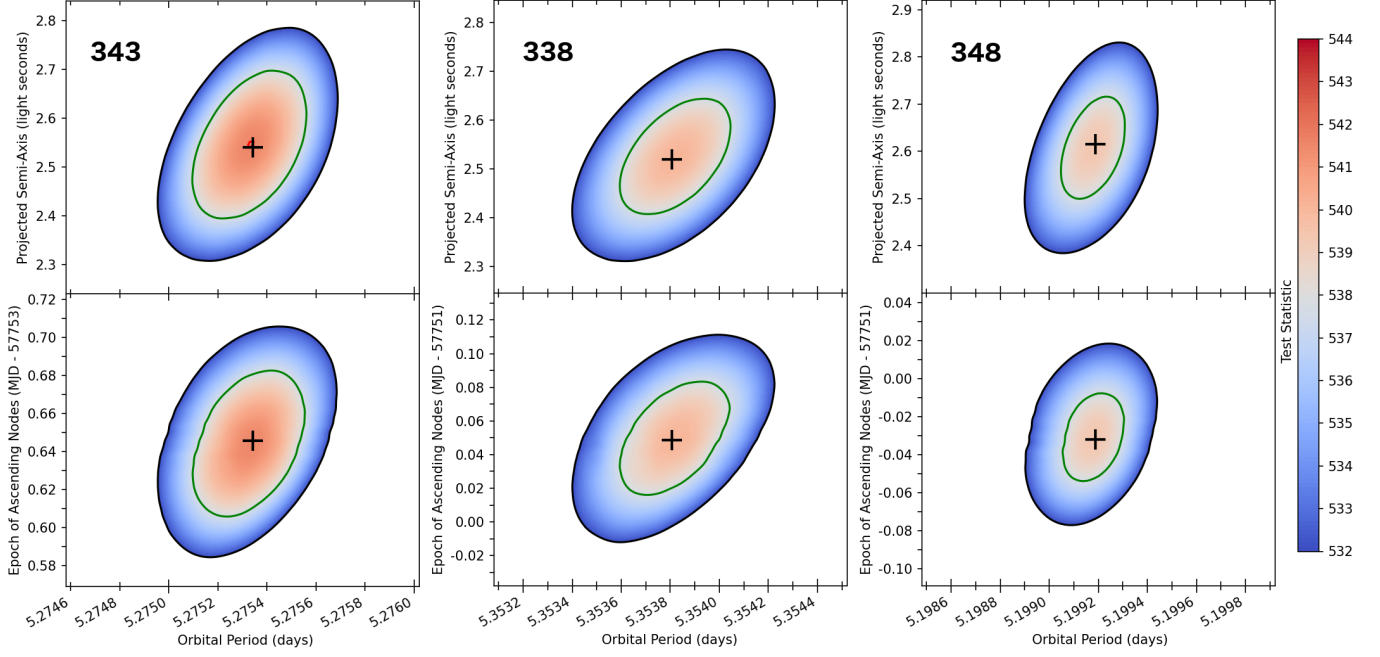
Figure 5. Estimates of the orbital parameters for the aliases labelled with IDs 343, 338, and 348 in table 2, from left to right. See fig. 2 for more details.
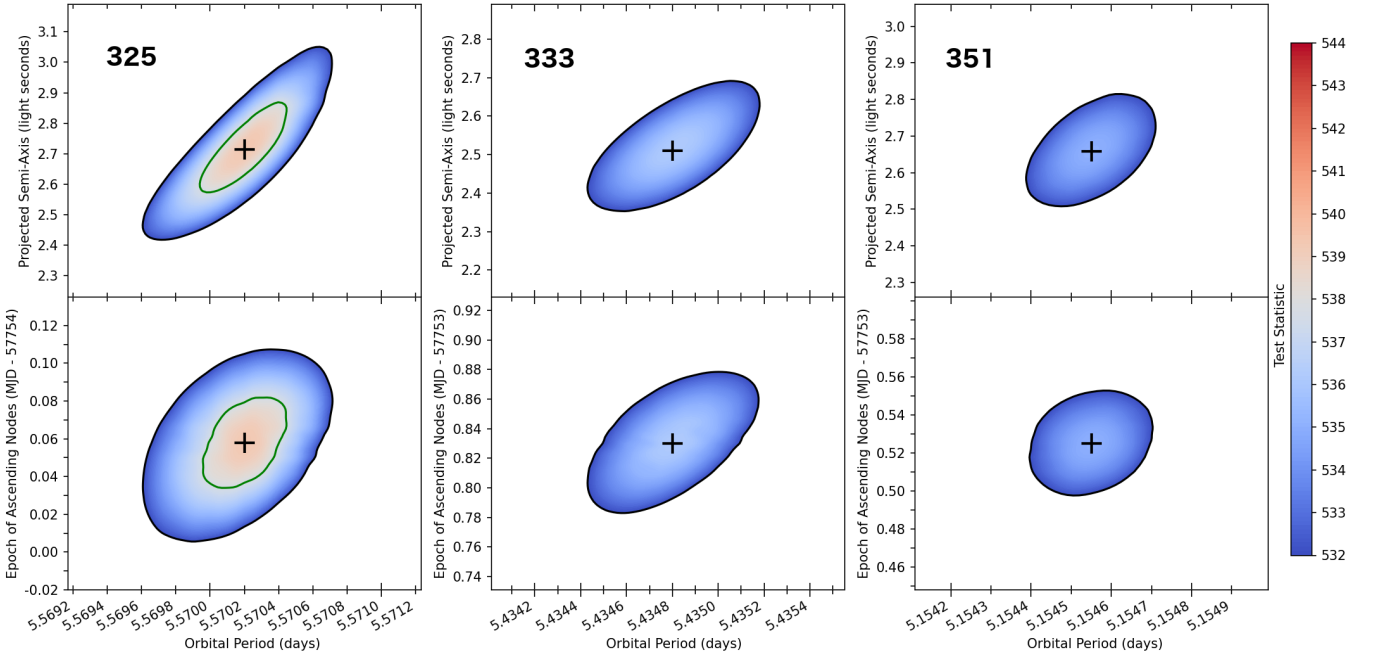
Figure 6. Estimates of the orbital parameters for the aliases labelled with IDs 325, 333, and 351 in table 2, from left to right. See fig. 2 for more details.

Cowan, G., Cranmer, K., Gross, E., & Vitells, O. 2011, European Physical Journal C, 71, 1554

Earnshaw, H. M., Roberts, T. P., Heil, L. M., et al. 2016, MNRAS, 456, 3840

Eggleton, P. P. 1983, ApJ, 268, 368

Eker, Z., Bakış, V., Bilir, S., et al. 2018, MNRAS, 479, 5491

Esposito, P., Israel, G. L., Belfiore, A., et al. 2016, MNRAS, 457, L5

Falanga, M., Bozzo, E., Lutovinov, A., et al. 2015, A&A, 577, A130

Fortin, F., García, F., Simaz Bunzel, A., & Chaty, S. 2023, A&A, 671, A149

Fürst, F., Walton, D. J., Harrison, F. A., et al. 2016, ApJL, 831, L14

Fürst, F., Walton, D. J., Heida, M., et al. 2021, A&A, 651, A75

Fürst, F., Walton, D. J., Israel, G. L., et al. 2023, A&A, 672, A140

Gabriel, C., Denby, M., Fyfe, D. J., et al. 2004, in Astronomical Society of the Pacific Conference Series, Vol. 314, Astronomical Data Analysis Software and Systems (ADASS) XIII, ed. F. Ochsenbein, M. G. Allen, & D. Egret, 759

Harrison, F. A., Craig, W. W., Christensen, F. E., et al. 2013, ApJ, 770, 103

Heida, M., Harrison, F. A., Brightman, M., et al. 2019, ApJ, 871, 231

Hou, X., Ge, M. Y., Ji, L., et al. 2022, ApJ, 938, 149

Hu, C.-P., Ueda, Y., & Enoto, T. 2021, ApJ, 909, 5

Israel, G. L., Belfiore, A., Stella, L., et al. 2017a, Science, 355, 817

Israel, G. L., Papitto, A., Esposito, P., et al. 2017b, MNRAS, 466, L48

Jansen, F., Lumb, D., Altieri, B., et al. 2001, A&A, 365, L1

King, A., & Lasota, J.-P. 2016, MNRAS, 458, L10

King, A., Lasota, J.-P., & Middleton, M. 2023, NewAR, 96, 101672

Liu, J., Vasilopoulos, G., Ge, M., et al. 2022, MNRAS, 517, 3354

Liu, Q. Z., van Paradijs, J., & van den Heuvel, E. P. J. 2005, A&A, 442, 1135

Martayan, C., Frémat, Y., Hubert, A. M., et al. 2006, A&A, 452, 273

Martins, F., Schaerer, D., & Hillier, D. J. 2005, A&A, 436, 1049

Neumann, M., Avakyan, A., Doroshenko, V., & Santangelo, A. 2023, A&A, 677, A134

Pike, S. N., Harrison, F. A., Bachetti, M., et al. 2019, ApJ, 875, 144

Pinto, C., & Walton, D. J. 2023, arXiv e-prints, arXiv:2302.00006

Pintore, F., Zampieri, L., Stella, L., et al. 2017, ApJ, 836, 113

Quast, M., Langer, N., & Tauris, T. M. 2019, A&A, 628, A19

Rappaport, S., & Joss, P. C. 1997, ApJ, 486, 435

Rappaport, S., Podsiadlowski, P., Joss, P. C., Di Stefano, R., & Han, Z. 1995, MNRAS, 273, 731

Rodríguez Castillo, G. A., Israel, G. L., Belfiore, A., et al. 2020, ApJ, 895, 60

Strüder, L., Briel, U., Dennerl, K., et al. 2001, A&A, 365, L18

Sutton, A. D., Roberts, T. P., Gladstone, J. C., et al. 2013, MNRAS, 434, 1702

Tauris, T. M., & van den Heuvel, E. P. J. 2023, Physics of Binary Star Evolution. From Stars to X-ray Binaries and Gravitational Wave Sources (Princeton University Press), doi:10.48550/arXiv.2305.09388

Townsend, L. J., Kennea, J. A., Coe, M. J., et al. 2017, MNRAS, 471, 3878

Tranin, H., Webb, N., Godet, O., & Quintin, E. 2023, arXiv e-prints, arXiv:2304.11216

Tsygankov, S. S., Doroshenko, V., Mushtukov, A. A., Lutovinov, A. A., & Poutanen, J. 2018, MNRAS, 479, L134

Vasilopoulos, G., Koliopanos, F., Haberl, F., et al. 2021, ApJ, 909, 50

Vasilopoulos, G., Ray, P. S., Gendreau, K. C., et al. 2020, MNRAS, 494, 5350

Walton, D. J., Mackenzie, A. D. A., Gully, H., et al. 2022, MNRAS, 509, 1587

Walton, D. J., Harrison, F. A., Bachetti, M., et al. 2015, ApJ, 799, 122

Walton, D. J., Fürst, F., Bachetti, M., et al. 2016, ApJL, 827, L13

Walton, D. J., Fürst, F., Heida, M., et al. 2018, ApJ, 856, 128

Wilson-Hodge, C. A., Malacaria, C., Jenke, P. A., et al. 2018, ApJ, 863, 9